PAPER • **OPEN ACCESS**

Influence of exit configuration on the flow fields and oscillation characteristics inside and outside the fluidic oscillator

To cite this article: Ahmed M Abdulnaim *et al* 2019 *IOP Conf. Ser.: Mater. Sci. Eng.* **610** 012052

Influence of exit configuration on the flow fields and oscillation characteristics inside and outside the fluidic oscillator

Ahmed M Abdulnaim[1,3], Ahmed A Emara[1,2] and Hany A Moneib[1]

[1] Department of Mechanical Power Engineering, Faculty of Engineering at El-Mataria, Helwan University, Cairo, 11718, Egypt
[2] Department of Mechanical Engineering, Faculty of Engineering, Bader University in Cairo (BUC), Cairo, 11829, Egypt

[3] Corresponding author: ahmed-abdulnaim@m-eng.helwan.edu.eg

Abstract. The fluidic oscillator shows very promising outcomes as an actuator in active flow control applications as it features several characteristics including no-moving parts, self-excitation, rigidity and reliability. The fluidic oscillator can be utilized in diverse applications including active-control of combustion and flow separation. The present work investigates the exit configuration influence on the flow dynamics of a small-scale double-feedback fluidic oscillator. Three configurations were modelled to examine the effects of the inclusion of a splitter inside the exit channel as well as the whole elimination of both the exit channel and splitter. Experimental results were obtained using particle image velocimetry (PIV) laser system with water as a working fluid and time-resolved pressure measurements using a hydrophone. Two-dimensional computational models based on Unsteady Reynolds-averaged Navier-Stokes (URANS) equations and shear stress transport (SST) were utilized considering the flow to be turbulent, incompressible, and isothermal. The results indicate that the exit configuration has no significant effects on the frequencies, while the jet deflection angle of the outflowing jet increases and the jet tends to be continuous when the splitter is removed. The splitter increases the outflow fluctuation amplitudes which would be suitable for diverse applications.

1. Introduction

Fluidic oscillators are recent interested subject within many scientific communities as actuators in the field of active flow control. These actuators has no moving parts, do not need an external power source and produce an oscillating jet when subjected to a pressurized fluid, [1]. The oscillations' nature is based on several fluid instabilities inside the device that govern the features of the emanating jet; such as frequency and jet deflection angle, [2]. This nature makes fluidic oscillators potentially attractive for use in active flow control applications. These applications could be found in many fields including; combustion, aerodynamics, and heat transfer. The work of fluidic oscillators in an active combustion control enables the achievement of better flame stability and reduced emissions, which are coupled with enhanced jet engines propulsion and performance, [3], [4], and [5]. These actuators are also used to control the flow separation over aerodynamic profiles; i.e. increase the aerodynamic performance of aircrafts by reducing the drag and increasing the lift, [6]. In the field of heat transfer,

fluidic oscillators have unsteady characteristics which make them eligible for the development of the next-generation heat exchangers with extremely high heat flux removal capacity, [7]. These actuators utilize fluidics technology, either via wall attachment mechanisms, called the Coanda effect (feedback fluidic oscillator), [8], and/or fluid interactions (feedback-free fluidic oscillator), [9]. There are two configurations of the feedback fluidic oscillators named as; single feedback and double feedback. The later configuration is shown in figure 1. It is comprised of an inlet port, a convergent nozzle, an oscillating chamber with two feedback channels on either side, a control throat and exit channel that may include a flow splitter.

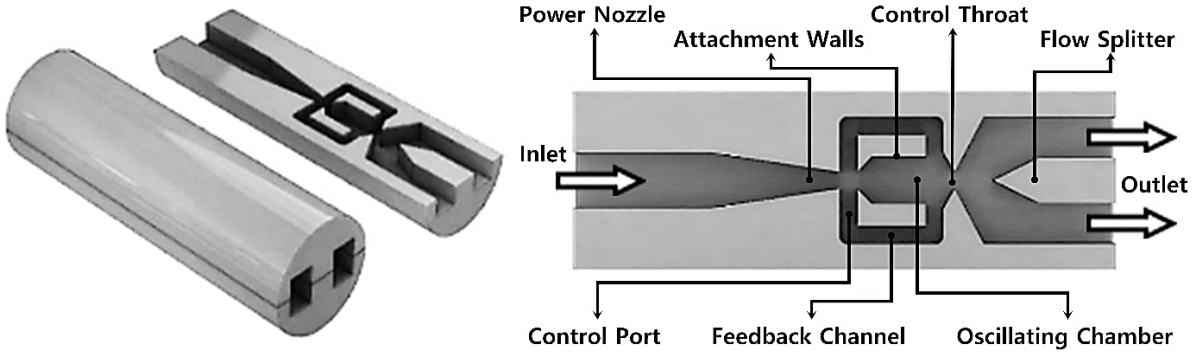

Figure 1. The double feedback fluidic oscillator.

The basic principle of a double feedback fluidic oscillator is the "Coanda effect". The oscillating jet is generated by supplying a pressurized fluid at the fluidics inlet. This pressurized fluid passes through a power nozzle; creating a jet flow at the entrance of the following oscillating chamber. Then the power jet expands to fill the chamber and the feedback channels. Coanda effect causes the power stream to attach to one of the two walls. Control throat allows a portion of the flow to enter the feedback channel which flows back to the control port and feeds the separation bubble causing the power stream to detach from the side wall. The power stream then switches to the opposite wall and the same process repeats; resulting in an oscillatory fluid motion inside the chamber. The sequence of operation is demonstrated in figure 2, [10].

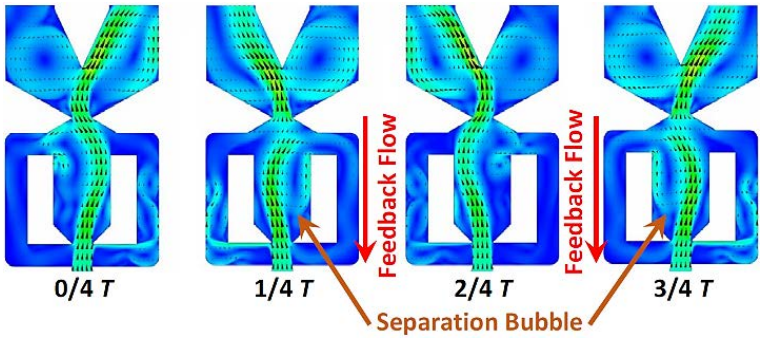

Figure 2. The sequence of operation of the double feedback fluidic oscillator.

Many experimental and computational studies were obtained on fluidic oscillators to understand the internal flow dynamics and oscillation phenomenon, and determine the parameters affecting the oscillation process. Previous studies, determined experimentally seven design modulation parameters that affect the oscillation period, [5] and [11]. Another study investigated the influence of internal geometry changes (feedback channel geometry including length and volume, mixing chamber inlet wedges, feedback channel inlet region, and the outlet region) on frequency and jet deflection angle of the fluidic oscillator. It was found that the diverging part of the outlet nozzle (control throat) has no influence on the inner flow structures of the oscillator, whereas the converging part of the outlet nozzle has a significant impact on the jet deflection angle. The feedback channels have lower

influence on the overall oscillation parameters, [12]. Other study investigated the effects of the roughness of the internal surfaces on the performance of a conventional curved fluidic oscillator. It has been observed that added surface roughness increases the oscillation frequency of the jet. Very little effect on the oscillation frequency has been observed for the rough feedback channel, [13]. At all these studies and others, the fluidic oscillator has undergone many experimental and numerical investigations to assess the internal and external flow fields. However, the internal flow of small-scale double feedback fluidic oscillators is very difficult to visualize experimentally because of small and complex geometries. Furthermore, a direct investigation of the influence of the exit configuration on the inner and outer flow fields was still lacking. In order to expand upon the current understanding of this point, different actuator models with different outlet configurations need to be studied. A research methodology was adopted to satisfy this investigation. It consists of experimental flow field and pressure measurements for the baseline model (named FX100) to provide experimental data for validation, then numerical simulations for the other models.

2. Approach

2.1. Investigated configurations

Three configurations were developed to study the influence of the exit geometry on the flow characteristics of the fluidic oscillator. These configurations differ from each other in the exit geometry. The baseline configuration was developed by reducing its size by 53.3% smaller than the original one used in [14] to meet insertion inside the EV-SSB and serving as a jet oscillator. This configuration is denoted as FX100. The second configuration is the same as FX100 but without the flow splitter at the exit and denoted as FX0. The last configuration is the same as FX100 but without splitter or exit channel and denoted as FX0'. These three configurations are shown in figure 3.

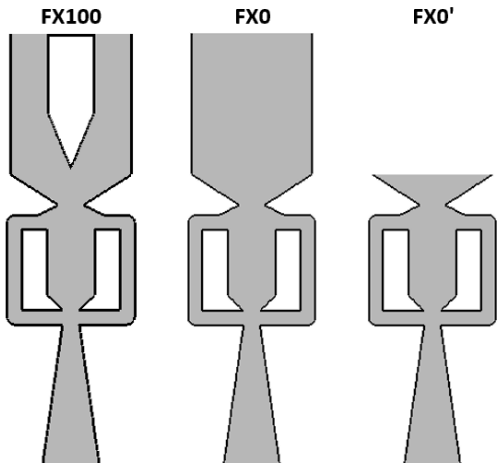

Figure 3. A schematic of the three fluidic oscillator configurations under investigation.

A study approach was developed to assess the impact of the fluidics exit configuration on the flow dynamics. The study comprised of experimental and numerical investigations. The baseline model FX100 was undergone experimental examinations to provide experimental data to validate the computational model. Then, the other two configurations were computationally investigated.

2.2. Experimental approach

In a small Plexiglas aquarium, the fluidic oscillator has been undergone into a series of hydrophone and PIV measurements. The aquarium dimensions were chosen as (60×30×40 cm) to suppress the walls' effect on the measured flow field. The aquarium was equipped with a small immersed water pump with a reasonable head, a rotameter with a maximum flowrate of 500 L/h, and a fine adjusting flow valve to pass the desired water flow to the fluidics. The aquarium was split into two zones; a

large zone for measurements and a small zone for pump suction. This arrangement guarantees; (i) a constant back-pressure head of the fluidics, (ii) suppressing the effects of the pump suction on the measured flow field. The whole test rig can be demonstrated in figure 4.

2.2.1. PIV setup. A standard Nd: YAG PIV laser system was used to generate a vertical laser sheet passing through the middle of the fluidic oscillator and parallel to flow direction inside it. The repetition rate was set to be 4 Hz, with a time interval between the two laser pulses 100 μs, to fit the flow velocity.

To track the flow correctly, a seeder consists of powder tracer ILA silver coated hollow glass spheres with mean particle size 15μm and micromer®-redF with mean particle size 6-10-12μm were utilized. To ensure homogeneous distribution of the tracers inside the aquarium, they were injected far upstream of the measurement plane.

The double frames were captured using ILA-CCD camera type: SensiCam, 12-bit cooled imaging with a resolution of 1280×1024 pixel. For a good investigation of the flow fields and increasing the spatial resolution, the camera was equipped with a 105mm focal lens Sigma optic. To subtract the surrounding light, a bandpass interference filter centered inside Hama C adapter (around 532 nm wavelength) was used.

Cross-correlation and adaptive cross-correlation algorithms were used with an interrogation window size of 16×16 pixel and 50% overlap for post-processing of the data with higher spatial resolution. To eliminate false vectors, filters of local median velocity and linear interpolation were utilized.

2.2.2. Hydrophone setup. A standard hydrophone, type RESON TC4013, was used to provide time-resolved pressure measurements of the flow oscillations outflowing from the fluidics under water inside the aquarium. This hydrophone can deal with a wide frequency range of 1Hz to 170kHz with high sensitivity (-211dB ±3dB re 1V/μPa at 1m). It also provides uniform unidirectional sensitivities in both vertical and horizontal planes up to high frequencies, [15]. The hydrophone was fixed in front of the fluidics where high signal amplitude was detected. The signals of the hydrophone were acquired using DAQ card and stored on a computer for post-processing i.e. applying FFT to generate the frequency spectrums.

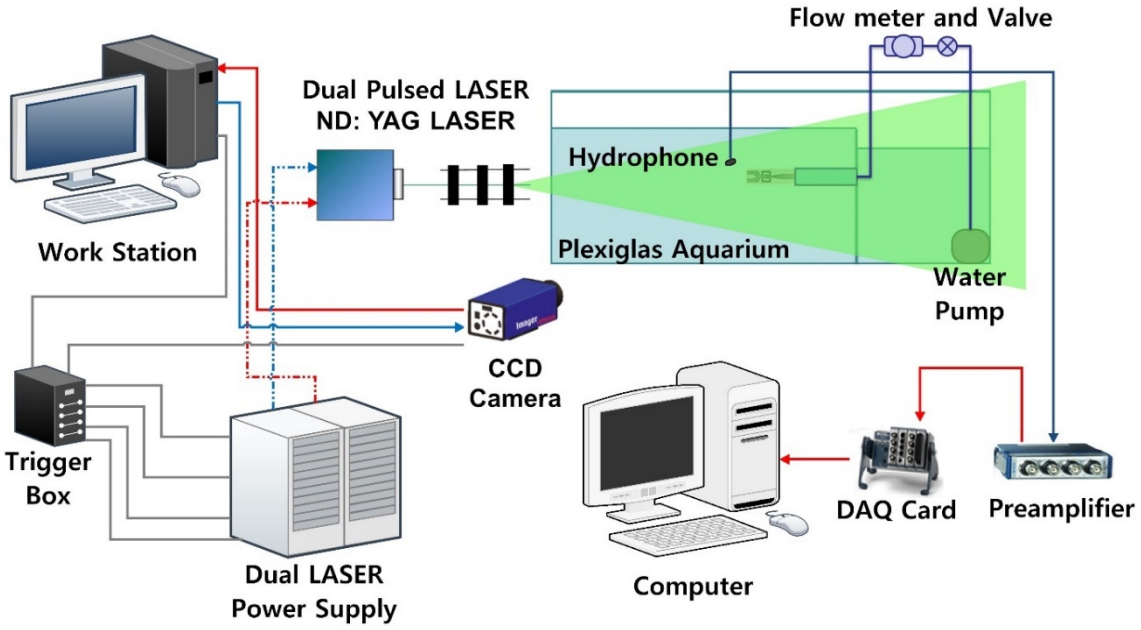

Figure 4. A full map of the schematic diagram of PIV and hydrophone measurement systems.

2.3. Numerical approach

To study the influence of the exit configuration on the fluidic oscillator flow fields, transient numerical simulations have been performed on 2-D meshes. The URANS equations are solved employing the SST turbulence model as provided in ANSYS CFX. It was found in a previous study that using a 2-D model based on URANS equations and employing the SST model is sufficient to describe the flow fields and oscillation characteristics qualitatively as well as quantitatively, [16]. The simulations were accomplished using the commercial licensed software ANSYS 18.1 Workbench. The CFX analysis system was used to conduct the simulations. The geometries and grids were modeled using ANSYS Geometry and Meshing modules.

2.3.1. Geometry preparation. To investigate the influence of the exit configuration on outer flow fields, the computational domain was extended by a rectangle ($10D_h \times 10D_h$), as shown in figure 5. The boundary condition of the sides of the rectangle was chosen to be an opening to allow the flow to enter or leave the domain. To make the model Independent of the inlet boundary conditions, an inflow section was added to the upstream of the oscillator ($10D_h$), [16]. Three geometries were developed to match the three configurations which were mentioned in section 2.1.

2.3.2. Mesh generation. All grids are two-dimensional block-structured meshes based on hexahedral finite volumes. CFX solver is not able to deal with pure two-dimensional grids, so, all grids were extruded by one cell thickness in normal direction to match the requirements of the solver. All grids were refined at high-velocity gradient zones as it was observed in the experiments in the literature, also near wall zones to resolve the shear layers and flow separations.

Due to the fact that grid quality affects the level of uncertainty in numerical simulations, it is essential to check grid convergence. The examination of the grid convergence of a simulation is a straight-forward method for determining the ordered discretization error in a CFD simulation. Usually, when the numerical solution becomes less susceptible to the spatial resolution as the grid is refined, it can be said grid convergence is satisfied.

A grid study was carried out with three different grids to assess the influence of the spatial grid resolution. The three grids are denoted as "Coarse", "Baseline", and "Fine". Table 1 shows an overview of the performed meshes for the grid sensitivity analysis.

Table 1. Overview of the performed meshes for the grid sensitivity analysis.

	Coarse	Baseline	Fine
Grid points	141,706	206,916	388,466
Grid elements	69,927	102,305	192,798

2.3.3. Simulation set-up. The fluid was set as water with a temperature of 293 K. The flow was considered to be turbulent, incompressible, and isothermal. The inlet velocity was set to be 0.746 m/s, resulting in flow rate equals 87 L/h as it was used in [5]. This flow rate is equivalent to Re = 6337 as computed with the hydraulic diameter at the power nozzle exit. The boundary condition at the outlet was set as an opening to atmospheric pressure. The conditions of the walls were selected as non-slip walls. All these boundary conditions superimposed onto the computational domain can be shown in figure 5. The transient simulation started with a steady solution and conducted with a time step of 5×10^{-4}s, with about 5000 time-steps (total simulation time is 2.5s). Five points were selected to monitor velocity and pressure fluctuations, two points inside the oscillating chamber at the end of attachment walls, one point at the middle of the control throat, and two points at the outlets, one for each limb. These points superimposed onto the domain are shown in figure 6.

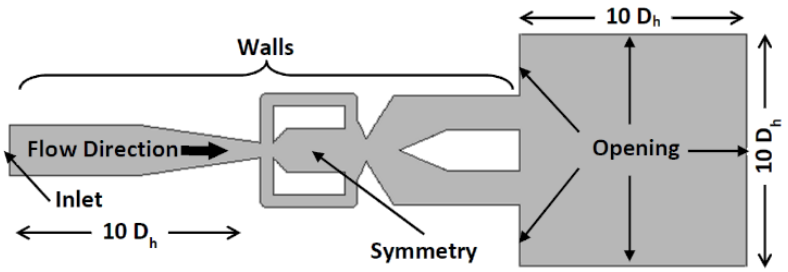

Figure 5. Boundary conditions superimposed onto the schematic of the computational domain for FX100 model.

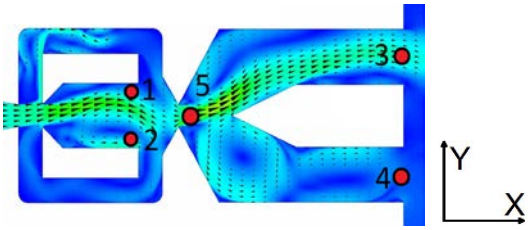

(1) IU: inner upper point (oscillating chamber)
(2) IL: inner lower point (oscillating chamber)
(3) OU: outer upper point (upper limb)
(4) OL: outer lower point (lower limb)
(5) C: center point (control throat)

Figure 6. Definitions and locations of the monitoring points.

3. Results and Discussion

3.1. Linearity of the frequency

The frequencies and the amplitudes of the baseline model FX100 can be obtained out of the pressure signal of the hydrophone by applying FFT. A linear relation between Reynolds number and the fluidics frequency in Hz can be detected as (see figure 7). The amplitude is direct proportion with the water volume flow rate as shown in frequency spectrum, [11].

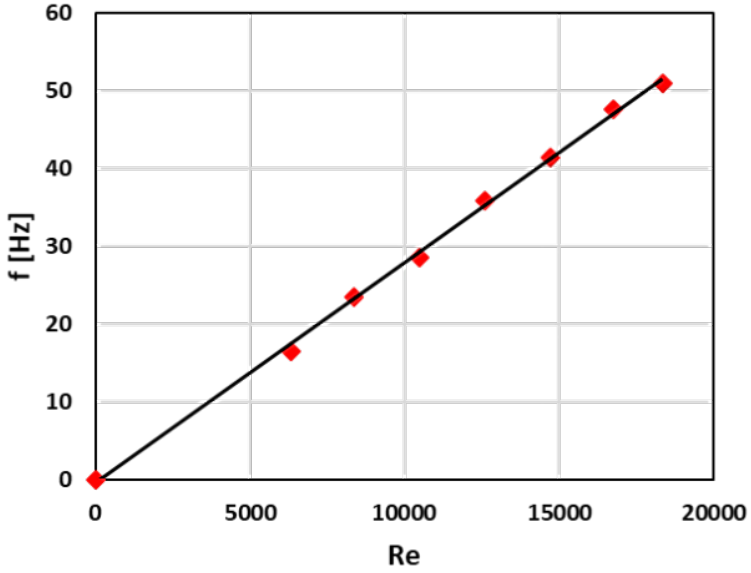

Figure 7. Fluidics frequency at different Reynolds numbers for configuration Fx100 as computed from the hydrophone signals.

3.2. Grid Convergence study

As declared in section 2.3.2, three different grids, including a coarse, a baseline, and a fine grid, are generated and used for the grid convergence study. Two-dimensional simulations are performed for a fixed inflow of 87 L/h on all three grids. The frequency of the oscillating jet is used as a measure of convergence because this is the key parameter for this kind of device. The streamwise velocity (u) fluctuation at the fluidics downstream exit limbs for every grid under study can be seen in figure 8.

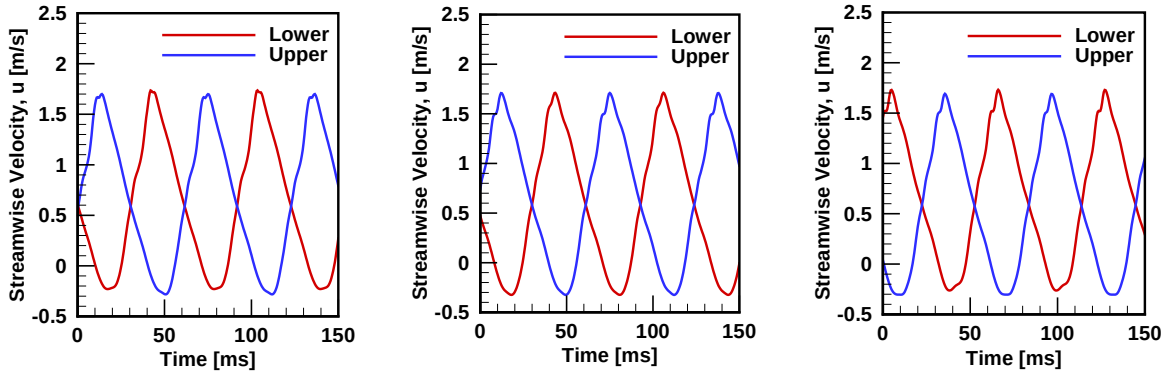

Figure 8. Streamwise velocity fluctuation at the fluidics exit limbs (lower and upper) for the three different grids.

In order to extract the dominant frequency of the oscillation, an FFT was applied to the instantaneous streamwise velocity signals of the three grids. The spectrum - figure 9 - shows that, all grids resulted in the same dominant frequency (16.11 Hz) making an error less than 1% of the measured frequency (16.25 Hz), but in the case of Baseline, the dominant frequency has a sharp and pure peak. This trait can be realized by observing the second harmonic peak which is at 32 Hz for Baseline, while Coarse and Fine grids have a second harmonic peaks shifted to 33 Hz. The sharpness and purity of the Baseline dominant peak led to having the maximum amplitude at both limbs, figure 9.

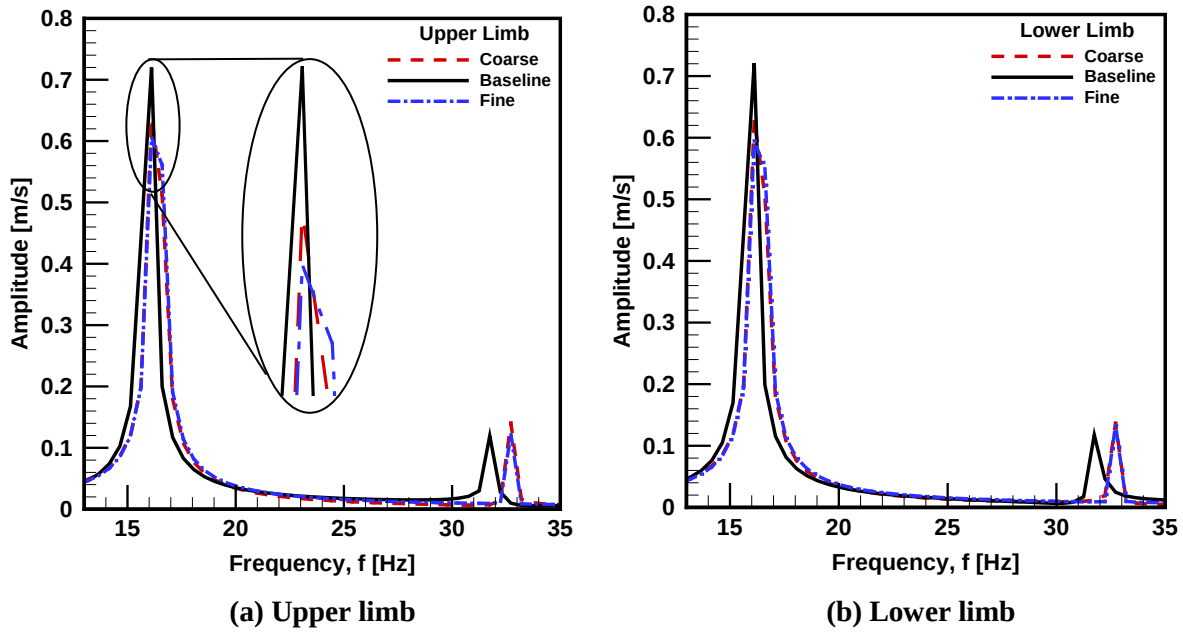

Figure 9. Fast Fourier transform of the streamwise velocity at points OU left and OL right for the three grids of the grid convergence study.

For all three grids, it is observed that the predicted dominant frequencies agree well with the measured value. Hence, it is assumed that the Baseline grid is independent of the grid resolution, therefore, it will be used in the other simulations. Table 2 compares the dominant frequencies and their amplitudes that resulted from the three grid resolutions at points OU and OL.

Table 2. Comparison of fluidics frequency resulted from the three grid resolutions.

Grid	Coarse		Baseline		Fine	
Exit Limb	Upper	Lower	Upper	Lower	Upper	Lower
Dominant frequency [Hz]	16.11	16.11	16.11	16.11	16.11	16.11
Amplitude [m/s]	0.637	0.630	0.720	0.721	0.606	0.595

3.3. Numerical Validation

The velocity components in a longitudinal cross section of FX100 for the PIV laser measurement system [11] and the simulation results at different phase angles can be shown in figure 10 and figure 11.

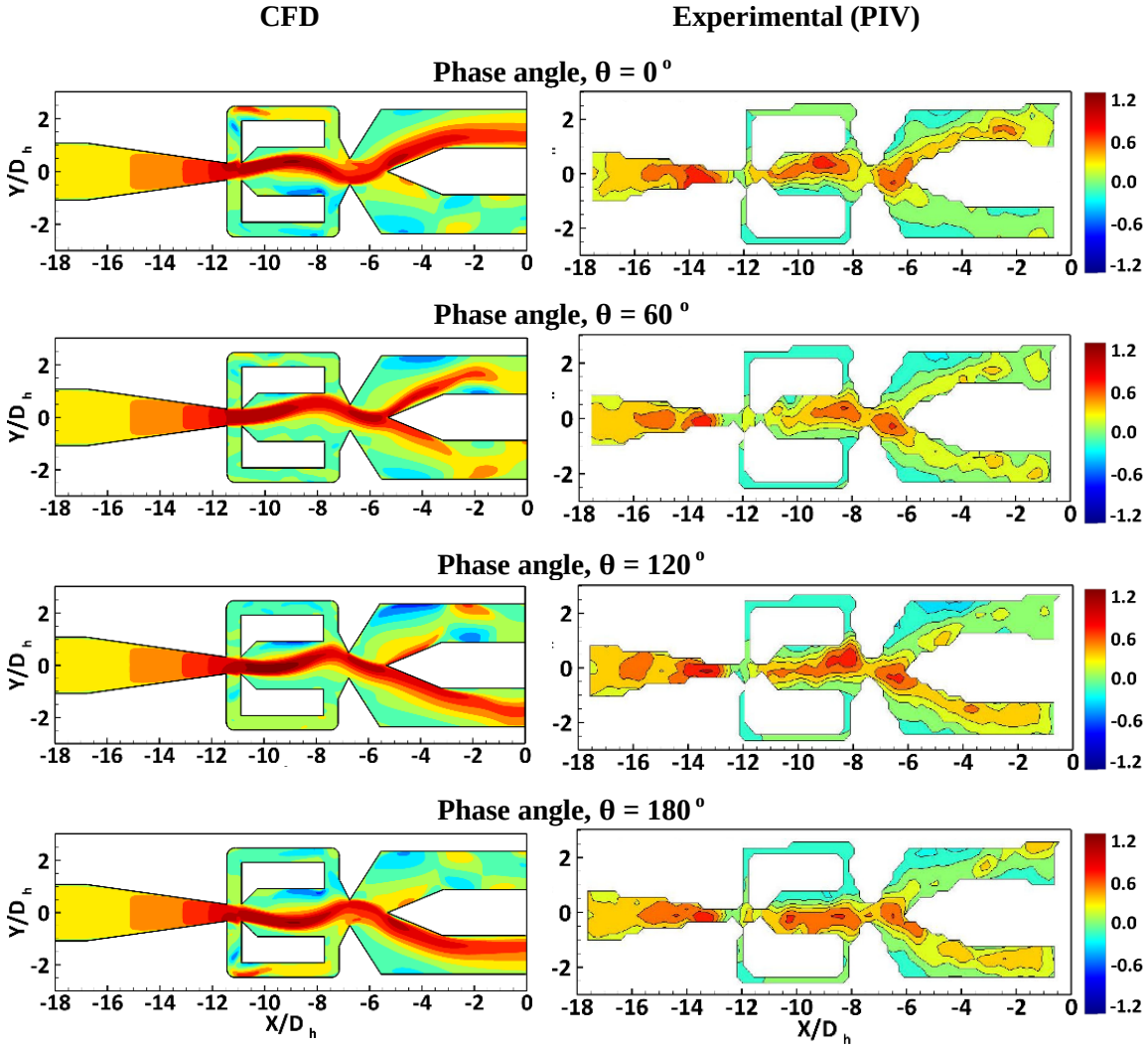

Figure 10. Validation between CFD (left) and PIV (right) [11] of the contours of streamwise velocity (u/U_B) for FX100 at Re = 6337 at different phase angles.

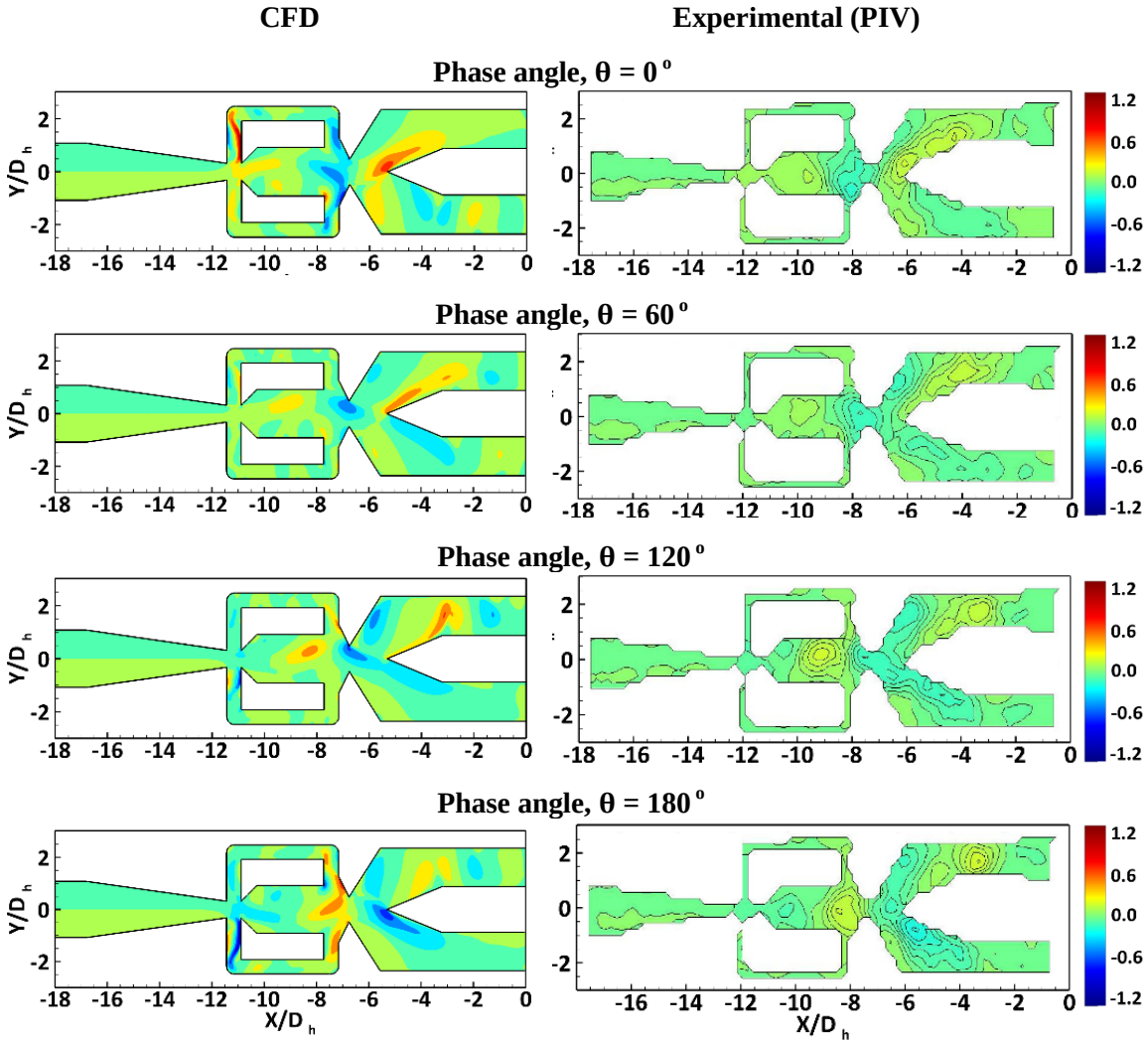

Figure 11. Validation between CFD (left) and PIV (right) [11] of the contours of radial velocity (v/U_B) for FX100 at Re = 6337 and at different phase angles.

By comparing the computed and the measured velocity contours, good similarities between contours can be observed. The completion of one cycle inside the oscillation chamber was determined as a complete phase, which was divided into 360 degrees (6 phase angles, one per 60 °). For a phase angle of θ = 0 °, the jet enters the actuator and directs firstly to the upper wall. The main jet leaves the oscillating chamber, while a small portion is guided through the lower feedback channel back to the power nozzle. There the feedback flow impinges the main jet and feeds the separation bubble in the oscillating chamber (θ = 60 °). With the growing separation bubble the main jet is deflected further upwards until it reaches its maximum at a phase angle of θ = 90 °. After that, the main jet feeds the opposite feedback channel and the process is re-initiated (θ = 120 ° and 180 °).

3.4. Flow analysis of the baseline model FX100

3.4.1. Flow field of baseline model FX100. The baseline model FX100 was simulated with an inlet flow rate of 87 L/min resulting in an oscillation frequency of 16.11 Hz. The velocity magnitude contours of FX100 at different phase angles can be shown in figure 12. One of the first things that can be observed from the figure is the increased velocity of the jet inside the oscillating chamber, reaching up to 1.2 U_B. While the jet at the upper limb has reached its maximum velocity in figure 12 (θ = 0 °),

the jet in the oscillating chamber is still pointing downward. It continues to move upwards till θ = 90 °, while the jet at the exit slowly moving downwards accordingly. When the jet in the oscillating chamber reaches the upper wall, it is deflected downwards, moving the exit jet to the lower limb in figure 12 (θ = 180 °). The jet inside the oscillating chamber moves from one side to the other by the effect of two main circulation zones (separation bubbles), which can grow and move aft by the returning flow flowing through the feedback loops. This mechanism was already visualized for a similar geometry by means of numerical simulations in [12] and PIV experiments in [11] and [17], showing very similar flow structures to what is presented here.

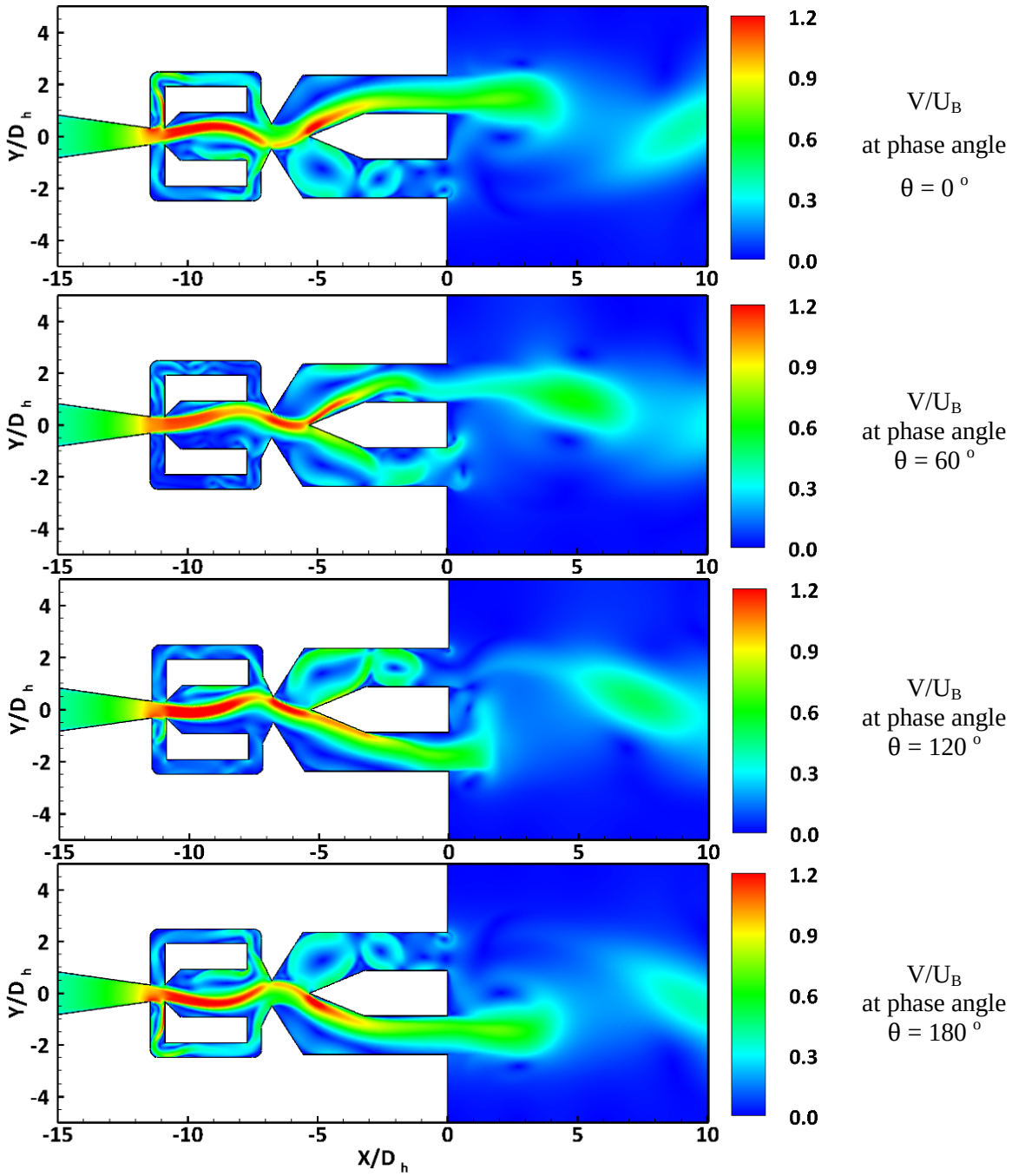

Figure 12. Velocity contour plots at different phase angles and Re = 6337 for the baseline model FX100.

The averaged velocity magnitude contours with the velocity vectors superimposed of baseline model FX100 can be shown in figure 13. The power nozzle causes an increase in velocities in the entrance of the oscillating chamber as shown in the figure. Then, the velocity distributes throughout the chamber, representing the oscillating jet. The average velocity of the flow in the feedback channels is limited to be zero, as the flow reflects its direction periodically. After passing the control throat, velocity magnitude increases, and the flow directs to the edge of the splitter. After that, the flow splits into two jets around the splitter which in turn form two recirculation zones behind. On both sides of the splitter, two small recirculation zones could be observed indicating the vortexes which are formed when the limb has a suction. At the outer flow field zone just behind the splitter, a zero-velocity region appears which represents a periodical weak vortex.

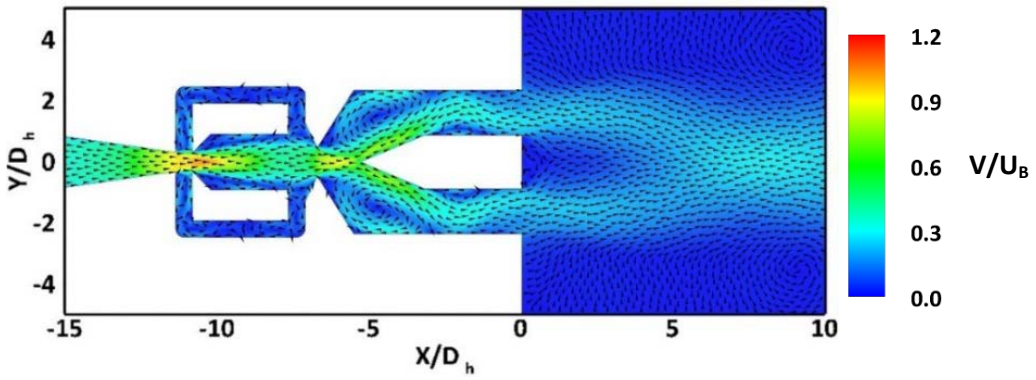

Figure 13. Average velocity magnitude contour plot with the velocity vectors superimposed at Re = 6337 for the baseline model FX100.

3.4.2. Frequency analysis of baseline model FX100. A single oscillation cycle of the streamwise velocity at the five monitored points for the baseline model FX100 can be shown in figure 14. The jet inside the oscillation chamber (points IU and IL) remains at the upper or lower attachment wall for a relatively long time (150 ^{o} or 42% of the cycle), before switching back to the other wall very quickly (30 ^{o} or 8% of the cycle). The dominant frequencies of the oscillating jet are computed from the streamwise velocity component at each point by applying FFT, see figure 15. The jet is oscillating inside the chamber with a frequency equal to 16.11 Hz for equivalent Reynolds number equal to 6337. At each time the jet gets attached to either wall, it leads to deflect the jet at the control throat (point C). This behaviour leads to double the oscillation of the jet at the control throat (31.74 Hz). Then, the jet returns to its first oscillation - inside the oscillation chamber - at the outlet limbs (points OU and OL).

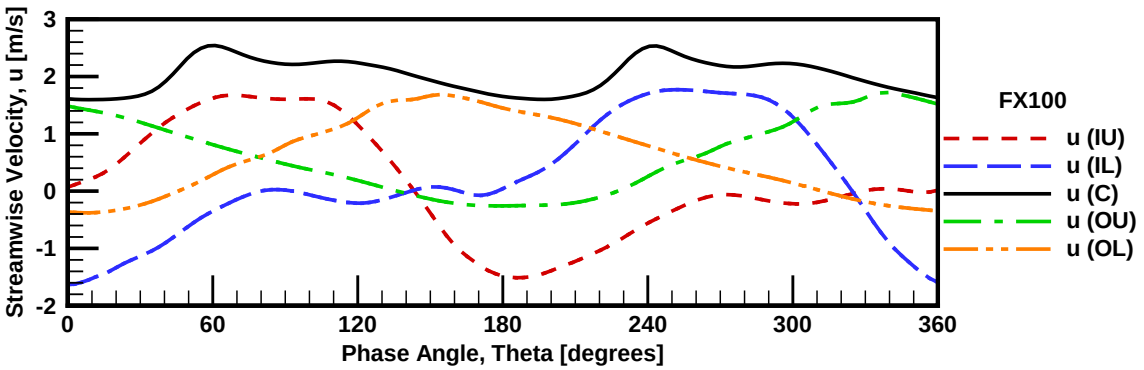

Figure 14. The streamwise velocity at the five monitoring points inside the fluidics and Re = 6337 for the baseline model FX100.

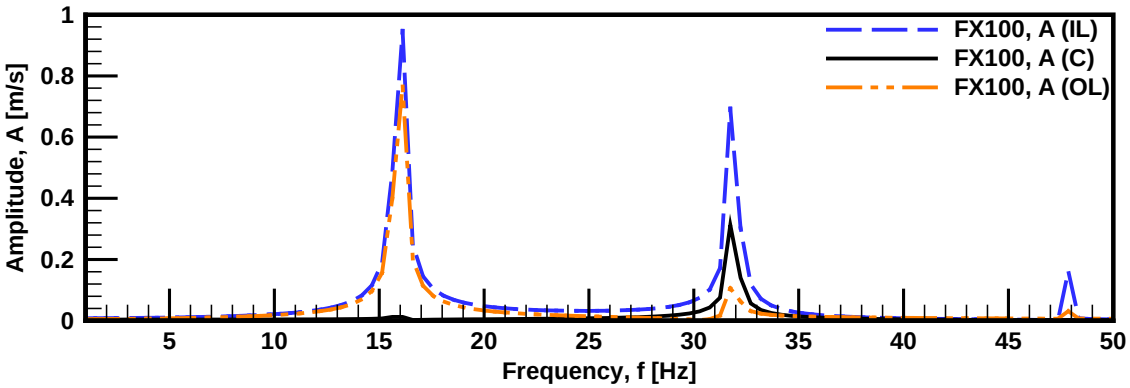

Figure 15. The Fast Fourier transform of the streamwise velocity signal at points (IL, C and OL) inside the fluidics with Re = 6337 for FX100.

3.5. The effect of outlet configuration

The two separate outlets configuration is useful for certain active flow control applications, but it may not be appropriate for all purposes. Some applications such as combustion control and mixing processes need pulsated jets, whilst other applications such as flow separation control need sweeping jets. So, the second configuration was modified by removing the flow splitter in the outlet section, whilst retaining the exit channel, so a confined sweeping jet can be obtained. While in the third configuration, the exit channel was also removed to produce a free sweeping jet.

3.5.1. Flow field comparison. To get a more elaborate insight of the exit configuration influence on the outer flow fields, the velocity magnitude contours for the three configurations are comparatively visualized at figure 16 and figure 17 at different phase angles. For the first configuration FX100, a Coanda effect appears at the splitter walls at the exit, which attaches the internal jet to one of the splitter sides and guides it to the corresponding limb, thus generating a high suction in the other limb. This suction makes the flow entered the actuator producing two main recirculation zones. Therefore, the outlet jet comes out sporadically as separated pulses (four separated pulses per cycle). This phenomenon is absent in the other configurations, as the splitter is removed. In the second configuration FX0, the splitter is principally removed, and the outlet jet is confined between the two sides of the exit channel, which in turn produces a large recirculation zone in the confined area. This recirculation zone locks up the jet for a quarter of the periodic time, producing equivalent two double pulses (a pair of two connected pulses) per cycle. In the last configuration FX0', the outlet jet is freely sweeping in front of the actuator. The jet seems to be continuous.

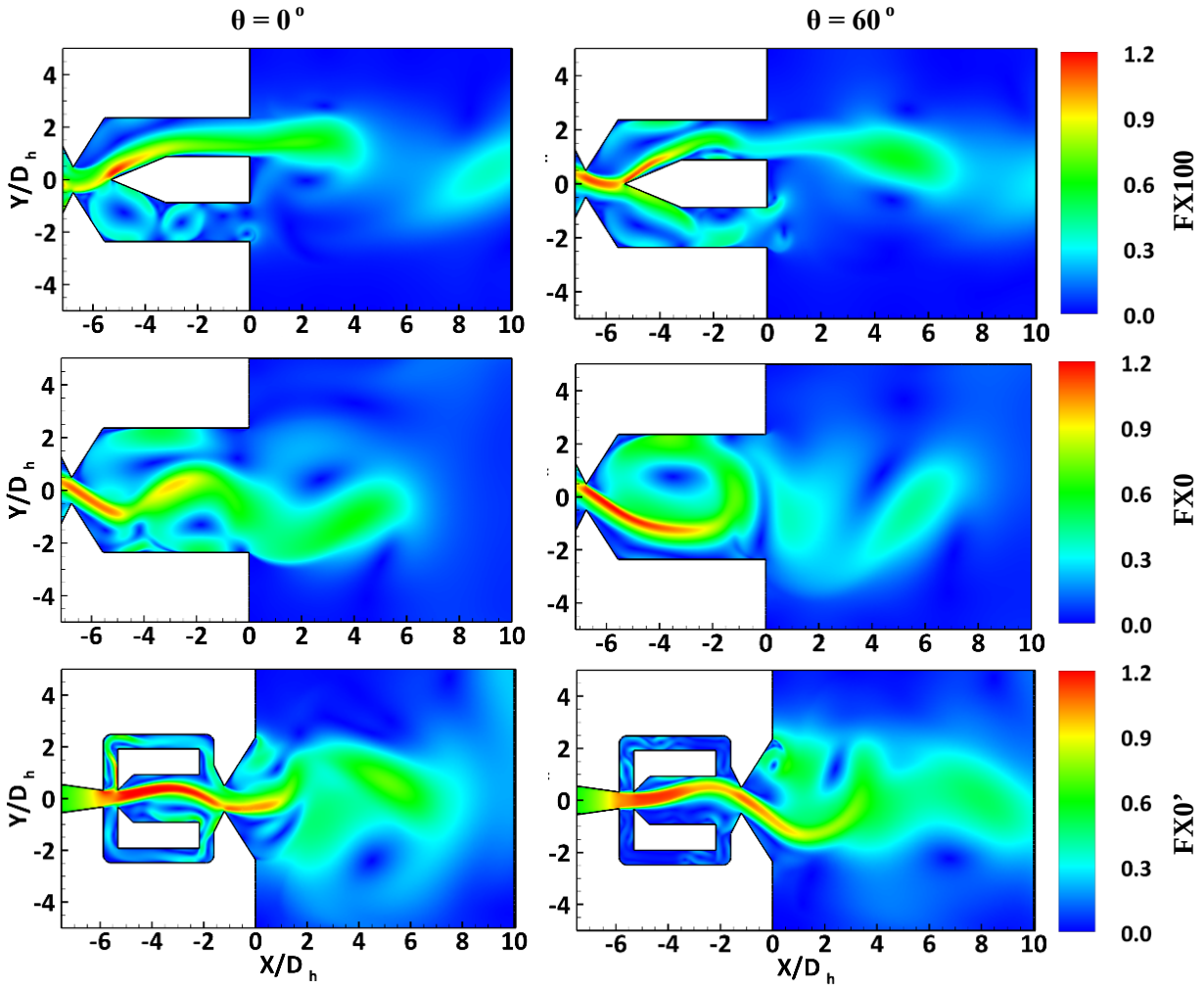

Figure 16. Velocity magnitude contour plots at phase angles θ = 0 ° and 60 ° and Re = 6337 for the three models under investigation.

3.5.2. Frequency comparison. A single oscillation cycle of streamwise velocity at the five monitored points for the model FX0 can be shown in figure 18. The streamwise velocity at point C (control throat) has a lower peak value than at the same point in the baseline model FX100, and the velocity fluctuation is flatter. From points OU and OL, the outlet jet speed is steady for a period of 90 ° (25% of the cycle). The Fast Fourier transform is applied on the streamwise velocity component at each point, see figure 19. The first observation is that the second harmonic peak at point IL has a lower and wider peak, where it reduced from 0.74 to 0.56 m/s. The same is for the dominant peak of point C. For the outlet jet (OL), all peaks have lower values than the baseline model FX100. This is due to the absence of the splitter, which expands the outlet area, thereby the jet velocity is reduced.

A single oscillation cycle of streamwise velocity and their corresponding frequency spectrum at the five monitored points for FX0' are shown in figure 20 and figure 21. The streamwise velocity fluctuation at point C seems to be flatter than FX100 and FX0 models, which is due to the absence of the outlet shoulder, thereby the outlet jet is freely sweeping with lower velocity magnitude and fluctuation amplitude. The internal jet fluctuates with a higher amplitude for the dominant frequency than the first two configurations. While, the second harmonic peak has a lower amplitude than them.

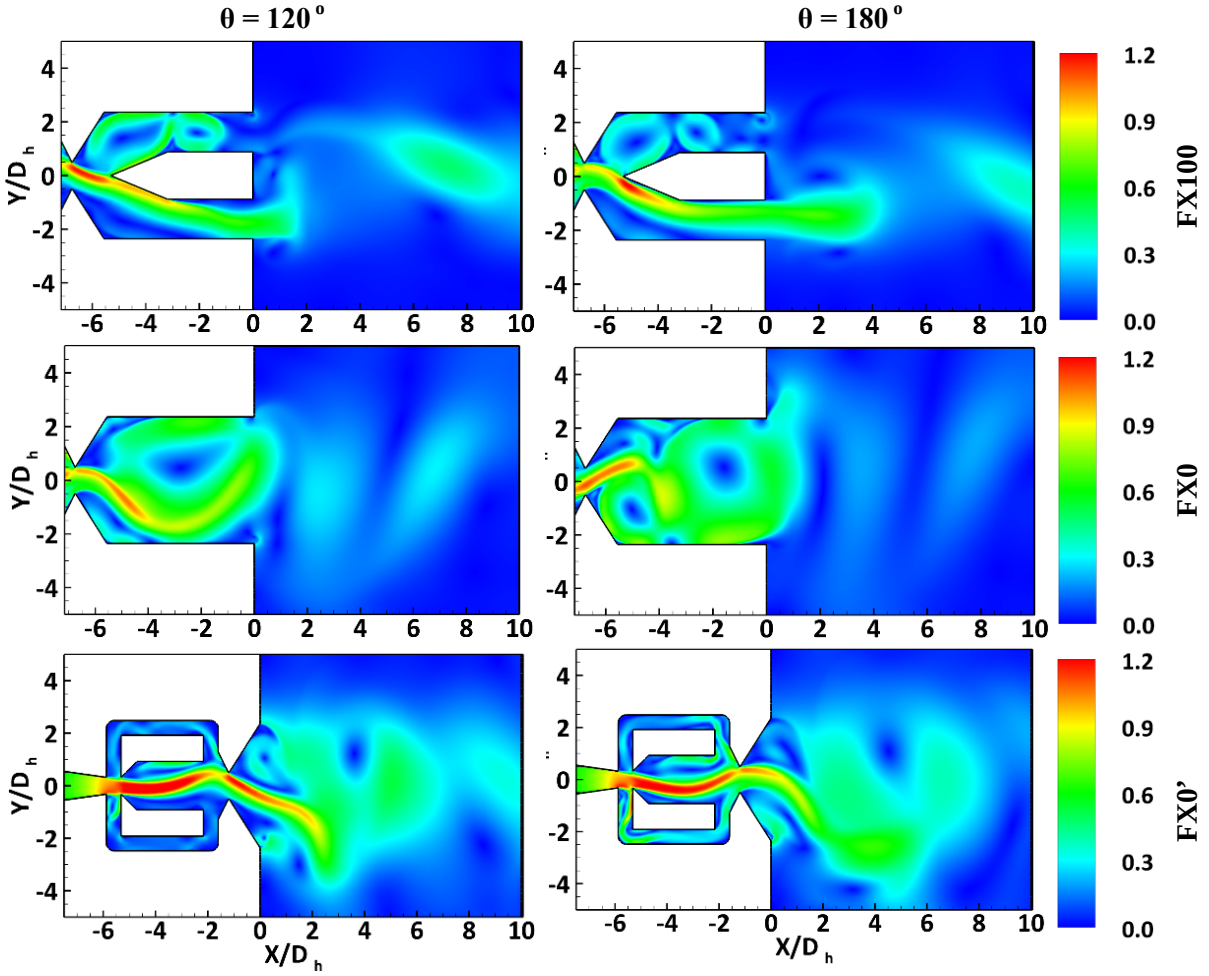

Figure 17. Velocity magnitude contour plots at phase angles θ = 120 ° and 180 ° and Re = 6337 for the three models under investigation.

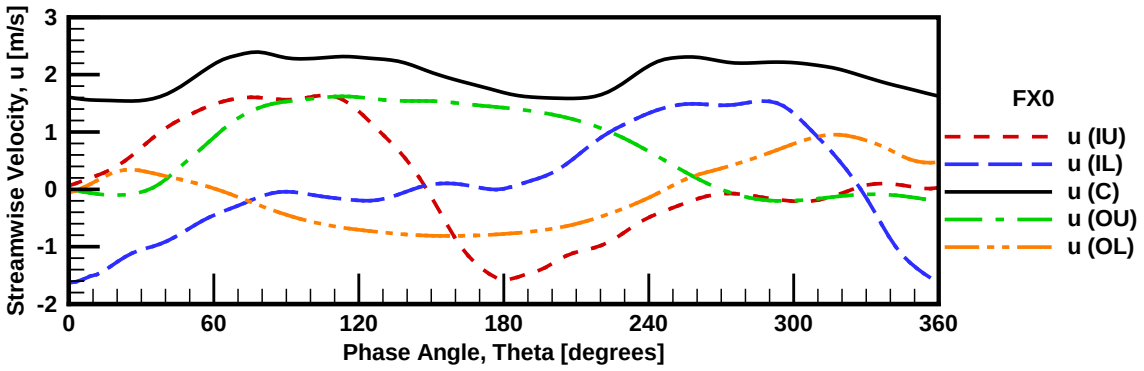

Figure 18. The streamwise velocity at the five monitoring points inside the fluidic oscillator at Re = 6337 for FX0.

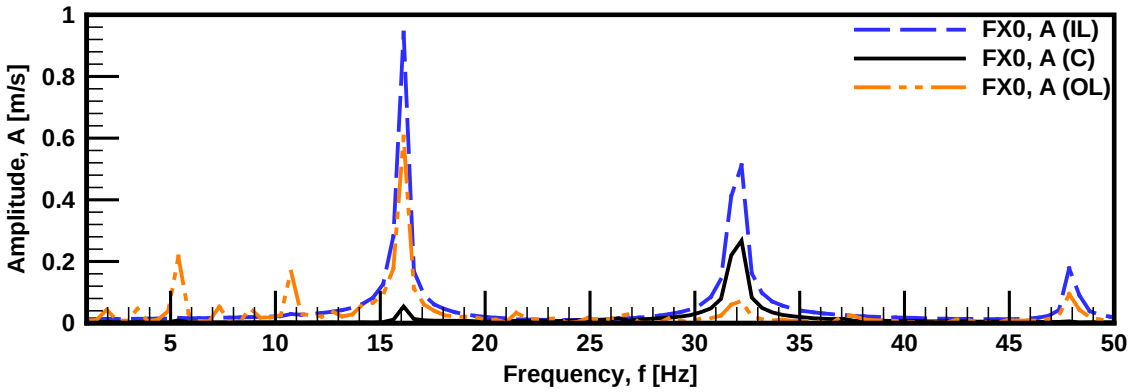

Figure 19. The Fast Fourier transform of the streamwise velocity signal at points inside the fluidic oscillator (IL, C and OL) at Re = 6337 for FX0.

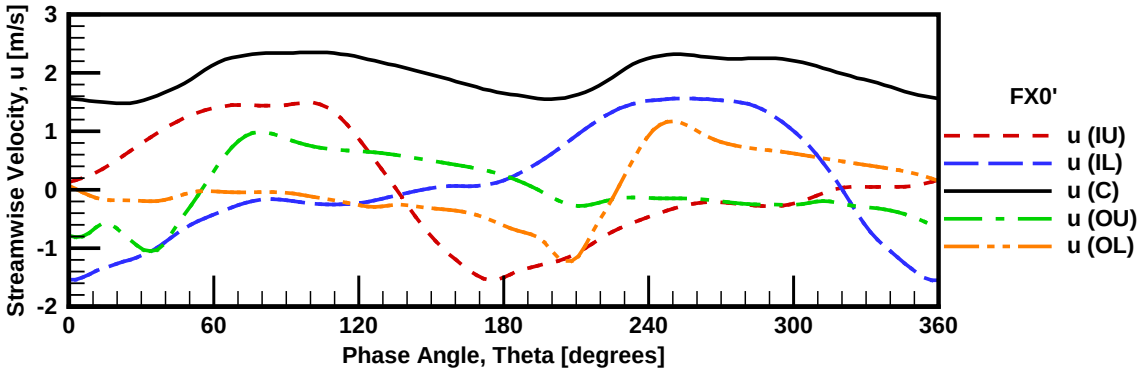

Figure 20. The streamwise velocity at the five monitoring points inside the fluidic oscillator and at Re = 6337 for FX0' model.

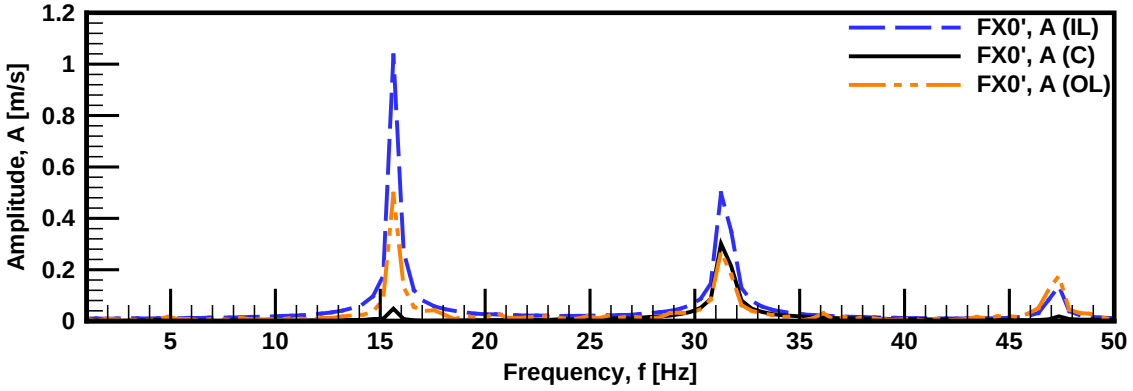

Figure 21. The Fast Fourier transform of the streamwise velocity signal at points inside the fluidic oscillator (IL, C and OL) at Re = 6337 for FX0'.

4. Conclusions

A small-scale double feedback fluidic oscillator has been undergone experimental and numerical investigations. Time resolved flowfields and pressure measurements using PIV laser system and hydrophone provide an experimental data to the process of validation. Unsteady simulations were performed on three models with different exit configurations to appraise the impact of the exit configuration on the inner and outer flowfields. A few key concluded remarks are listed below:

- Resolving the internal flowfields using PIV laser system measurement system was inadequate due to the complex and small geometries (feedback channels).

- The computational model results of the baseline model FX100 (with exit channel and splitter) showed a good matching with the experimental results with frequency error around 1%.
- The other two configurations FX0 (without splitter) and FX0' (without exit channel and splitter) were also simulated, and their flow mechanics, monitored velocities and their corresponding frequency spectrum were demonstrated.
- The existence of the splitter at the exit in the baseline model (FX100) led to produce separated pulses, which are adequate to some applications including active combustion control.
- The absence of the splitter in the FX0 configuration led to confine the outlet jet between the channel sides, which produced double pulses.
- When the exit channel was removed in the FX0' configuration, the outlet jet became a free sweeping jet, which is suitable for many applications of active flow control, like flow separation control.

References

[1] Cattafesta L N and Sheplak M 2011 Actuators for Active Flow Control *Annual Review of Fluid Mechanics* **43** 247–72
[2] Gregory J and Tomac M N 2013 A Review of Fluidic Oscillator Development and Application for Flow Control *43rd Fluid Dynamics Conference* (Reston, Virginia: American Institute of Aeronautics and Astronautics)
[3] Hassan S, Elkady M, Moneib H A, Omar A A, Emara A A, Attia A and Abdulnaim A M 2018 An Investigation of the Influence of Fluidics Insertion Technique on Argon Gas Additives to LPG on the Turbulent Lean Premixed Flame Characteristics for EV Burner *AMME-18 - Military Technical College, Cairo, Egypt*
[4] Bobusch B C, Berndt P, Paschereit C O and Klein R 2015 Investigation of Fluidic Devices for Mixing Enhancement for the Shockless Explosion Combustion Process *Active Flow and Combustion Control 2014* ed Rudibert King (Springer International Publishing) pp 281–97
[5] Emara A A 2011 *Interactions of Flow Field and Combustion Characteristics in a Swirl Stabilized Burner* (PhD Thesis, Technical University - Berlin)
[6] Phillips E, Jentzsch M P, Menge P M, Taubert L, Forster M and Wygnanski I J 2019 On the Use of Active Flow Control to Change the Spanwise Flow on Tailless Aircraft Models, Thus Affecting their Trim and Control *AIAA Scitech 2019 Forum* (Reston, Virginia: American Institute of Aeronautics and Astronautics)
[7] Wu Y, Yu S and Zuo L 2019 Large eddy simulation analysis of the heat transfer enhancement using self-oscillating fluidic oscillators *International Journal of Heat and Mass Transfer* **131** 463–71
[8] Coanda H 1934 Device for deflecting a stream of elastic fluid projected into an elastic fluid
[9] Raghu S 2001 Feedback-free fluidic oscillator and method 19
[10] Hossain M A, Prenter R, Lundgreen R K, Agricola L, Ameri A, Gregory J W and Bons J P 2017 Investigation of Crossflow Interaction of an Oscillating Jet *55th AIAA Aerospace Sciences Meeting* (Reston, Virginia: American Institute of Aeronautics and Astronautics)
[11] Emara A and Paschereit C O 2011 Fluidic Oscillator for Jet Streams Integrated into a Pilot Fuel Lance *7th Int. Symp. on Stratified Flows* (Rome, Italy)
[12] Bobusch B C, Woszidlo R, Krüger O and Paschereit C O 2013 Numerical Investigations on Geometric Parameters Affecting the Oscillation Properties of a Fluidic Oscillator *21st AIAA Computational Fluid Dynamics Conference* (Reston, Virginia: American Institute of Aeronautics and Astronautics)
[13] Hossain M A, Prenter R, Agricola L, Lundgreen R K, Ameri A, Gregory J W and Bons J P 2017 Effects of Roughness on the Performance of Fluidic Oscillators *55th AIAA Aerospace Sciences Meeting* (Reston, Virginia: American Institute of Aeronautics and Astronautics)
[14] Guyot D, Taticchi Mandolini Borgia P, Paschereit C O and Raghu S 2008 Active Control of Combustion Instability Using a Fluidic Actuator *46th AIAA Aerospace Sciences Meeting and*

Exhibit (Reno, Nevada: American Institute of Aeronautics and Astronautics)
[15] Teledyne RESON 2016 Hydrophone TC4013 - Miniature Reference Hydrophone
[16] Krüger O, Bobusch B C, Woszidlo R and Paschereit C O 2013 Numerical Modeling and Validation of the Flow in a Fluidic Oscillator *21st AIAA Computational Fluid Dynamics Conference* (Reston, Virginia: American Institute of Aeronautics and Astronautics) pp 1–13
[17] Bobusch B C, Woszidlo R, Bergada J M, Nayeri C N and Paschereit C O 2013 Experimental study of the internal flow structures inside a fluidic oscillator *Experiments in Fluids* **54** 1559